Electronic Supplementary Information

Phosphorylated Graphene Monolith with High Mixed Proton/Electron Conductivity

Li Cao [a,b], Hong Wu [a,b,c*], Zehua Mu [a,b], Xueyi He [a,b], Chongbin Wang [a,b], Jinzhao Li [a,b], Yan Li [a,b], Mingzhao Xu [a,b], Zhongyi Jiang [a,b*]

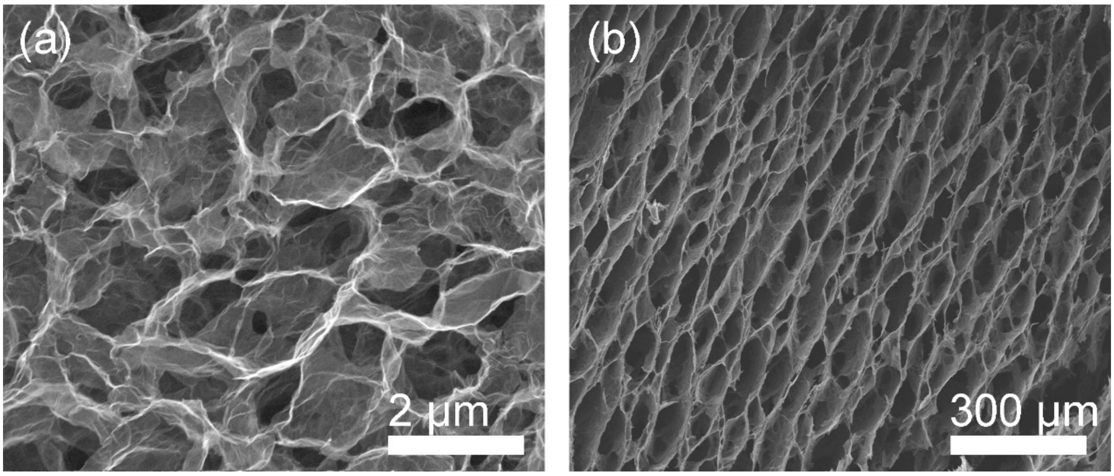

Fig. S1. SEM images of PGM prepared from the as-formed PGH: a) by the freeze-drying method, showing disordered structures; b) by the freeze casting method, showing long-range ordered structures.

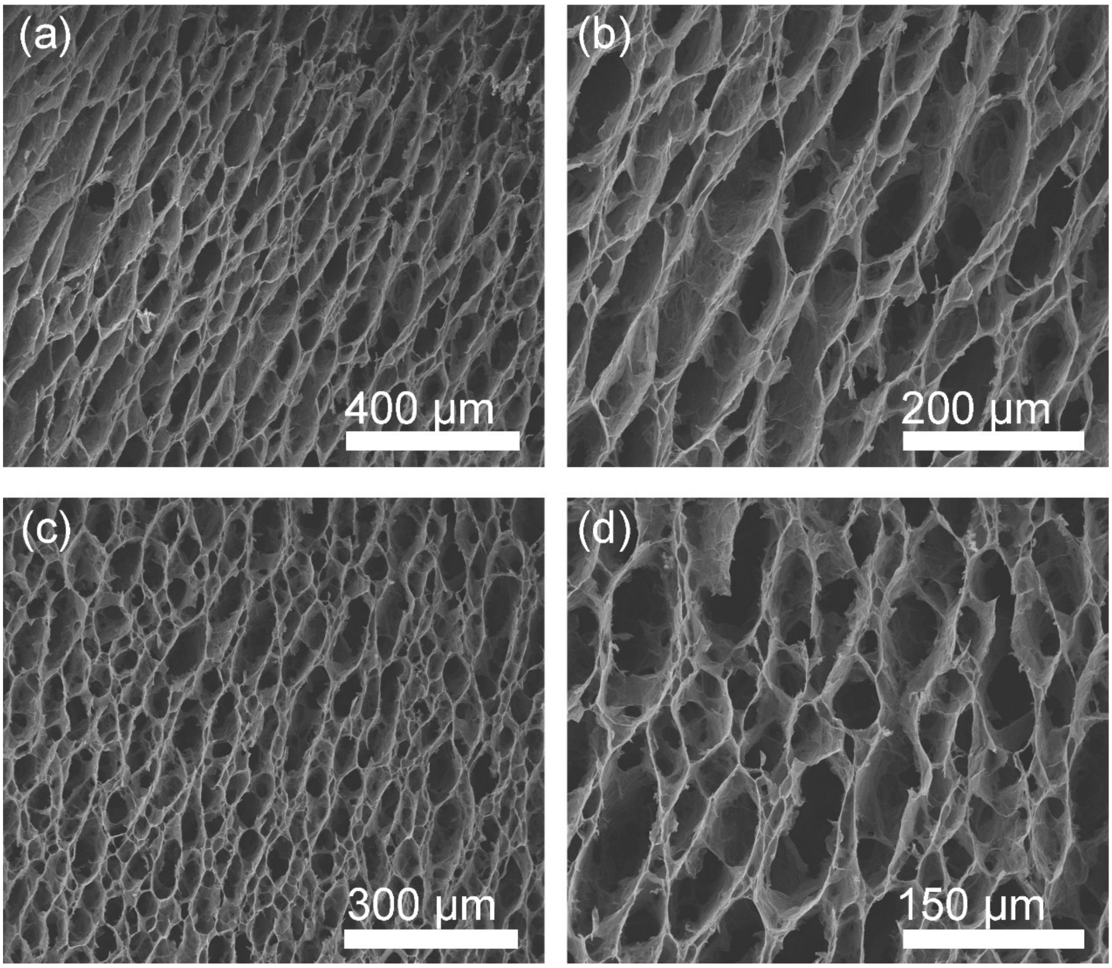

Fig. S2. SEM images of PGM prepared by the freeze casting method with different experimental parameters: a, b) PGM-1-12; c, d) PGM-1-16.

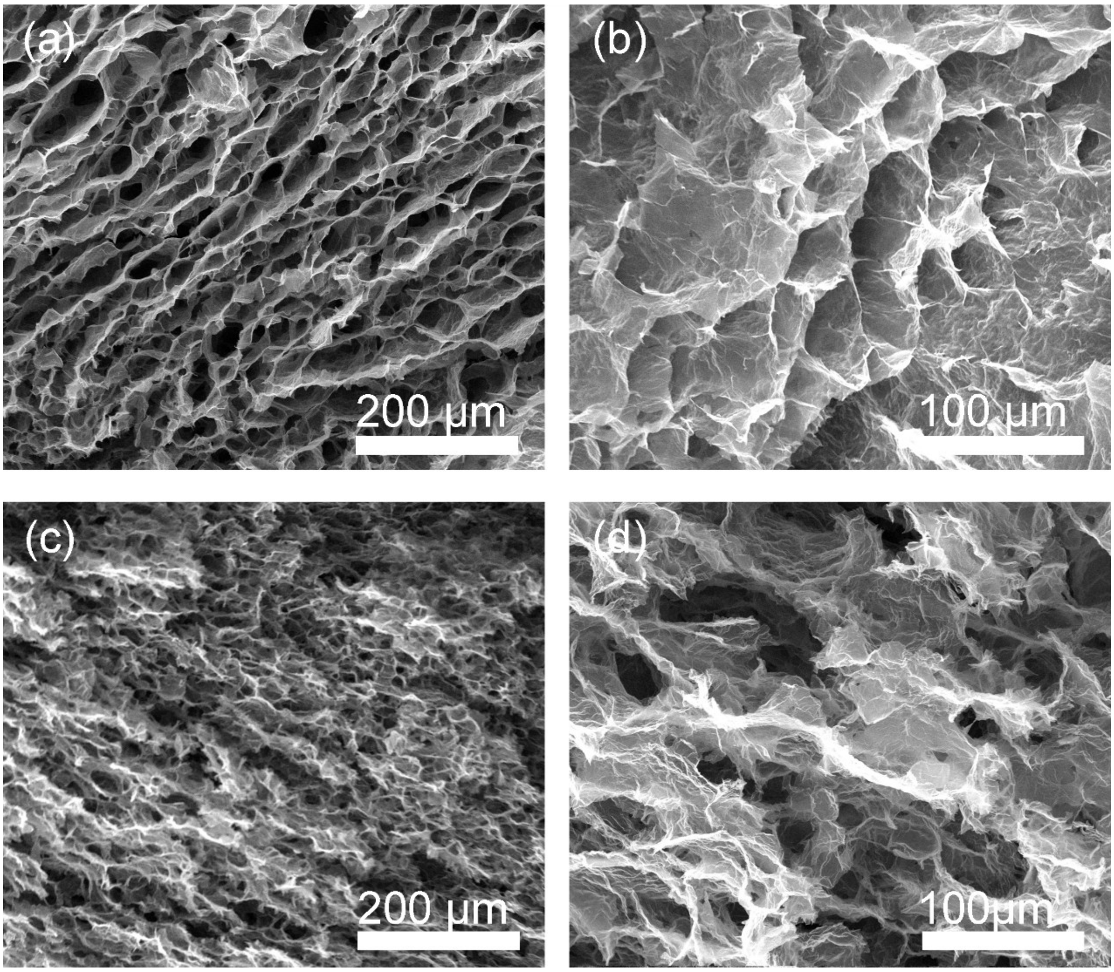

Fig. S3. SEM images of PGM prepared by the freeze casting method with different experimental parameters: a, b) PGM-1-30; c, d) PGM-2-24; Both samples exhibite small pore size and disorder structures.

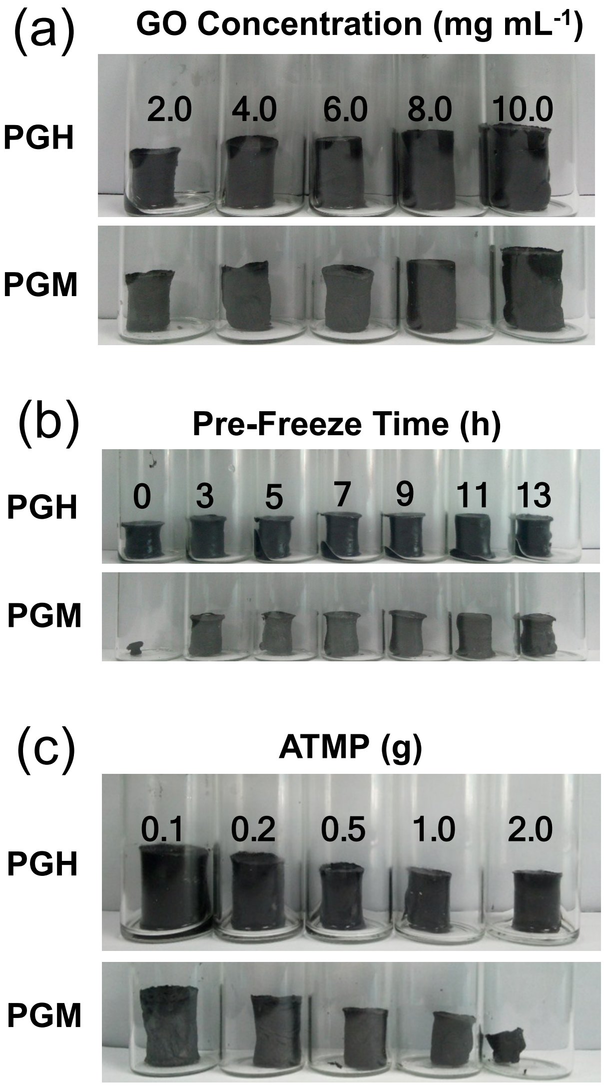

Fig. S4. The optical photographs of PGH and PGM with different experimental parameters.

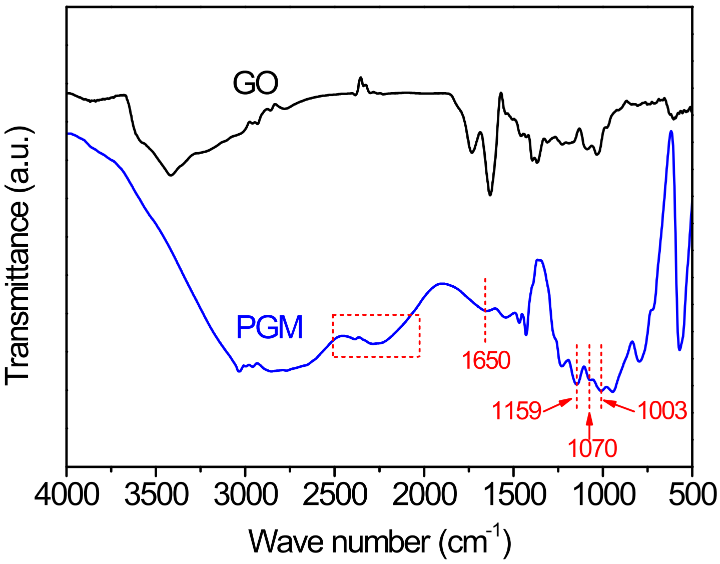

Fig. S5. FTIR spectra of GO and PGM

In general, the materials will exhibit mixed proton/electron conductivity when proton carriers are introduced into electronic conductors.[1-5] In the current work, the phosphate groups (proton carriers), which are able to construct interconnected hydrogen-bond networks for proton transport, were introduced into reduced graphene oxide (rGO) interlayers (electronic conductors). Therefore, the resulting phosphorylated graphene monolith (PGM) was expected to have mixed conductivity. The PGM with electron conductivity can be understood easily, since rGO is an electronic conductor. To provide a direct and solid proof for proton conductivity of phosphorylated graphene monolith, the hydrogen fuel cell performance using PGM as the proton-exchange membrane material and complex impedance analyses were carried out, as discussed in the following sections.

In hydrogen fuel cells, hydrogen is dissociated into electrons and protons at the anode. The protons must be transported to the cathode through a membrane (proton conductor), and the rejected electrons flow through the external circuit, which results in electronic power output. That means if the protons cannot be transported from anode to cathode, there will no electronic power output. Accordingly, the membrane should be proton-conducting and electron-insulating.

Phosphorylated graphene films (PGF) were sandwiched between two Nafion® membranes (commercial proton-conducting membrane) to make a composite membrane, denoted as Nafion-PG film-Nafion (N-PGF-N) (**Fig. S6a, b**). The N-PGF-N composite membrane is electron-insulating, because the Nafion® membrane is unable to transport electrons. If the N-PGF-N composite membrane is proton-conducting, we can deduce that the PGF is a protonic conductor.

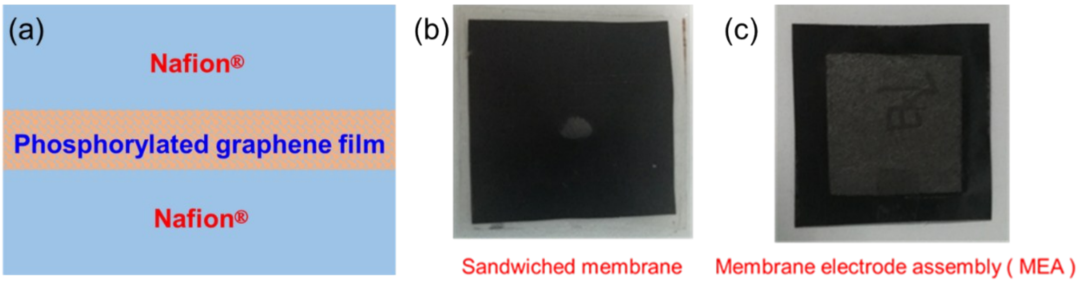

Sandwiched membrane

Membrane electrode assembly (MEA)

Fig. S6. Schematic illustration of sandwiched membrane (a); the optical photograph of sandwiched membrane (b) and membrane electrode assembly (c).

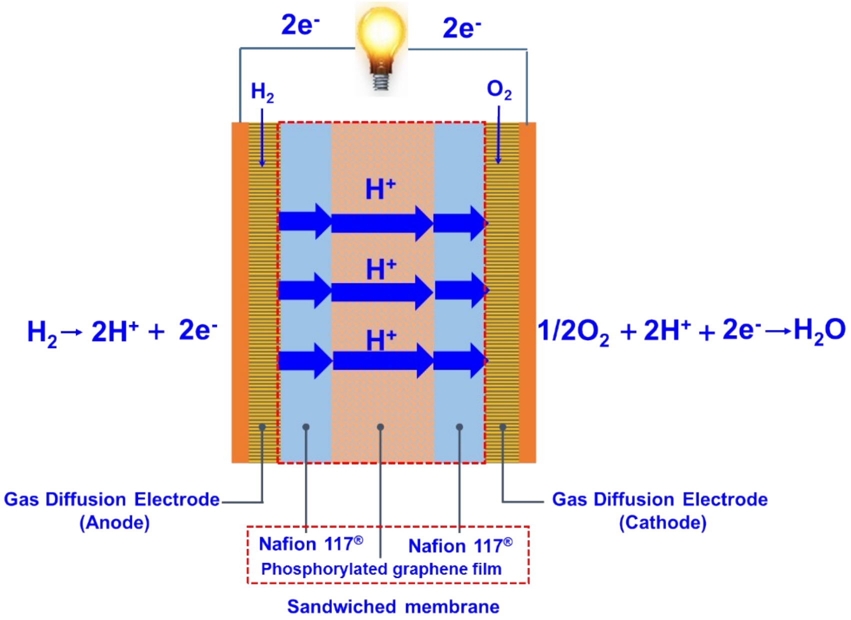

Fig. S7. H_2/O_2 fuel cell with Nafion-PG film-Nafion composite membrane.

Then, we made a membrane electrode assembly (MEA) using the N-PGF-N composite membrane (**Fig. 6c**). The H_2/O_2 single cell performance of N-PGF-N composite membrane was tested at 60 ^{o}C under 100% RH (**Fig. S7**). The polarization curves and power density curves were shown in **Fig. S8**. The maximum power density of the fuel cell with N-PGF-N composite membrane is ~70 mW cm^{-2}, which indicated that the N-PGF-N composite membrane is proton-conducting. Therefore, the PGF is a protonic conductor. To make a clearer clarification of the proton-conducting feature of PGF, the rGO film was also sandwiched between two Nafion® membranes to fabricate a Nafion-rGO film-Nafion (N-rGOF-N) composite membrane (**Fig. S9a**), and then we tested the H_2/O_2 single cell performance (**Fig. S9b**). As shown in **Fig. S8**, an ultralow power density (~1 mW cm^{-2}) could be found, because the N-rGOF-N composite membrane has very low proton conductivity. Besides, this obvious current flow indicates that rGO has contribution to the proton conductivity of the PGM as well. The proton-conducting feature of rGO may be attributed to the remaining oxygen-containing groups on rGO surface, which endows rGO with additional proton transport sites.[6, 7]

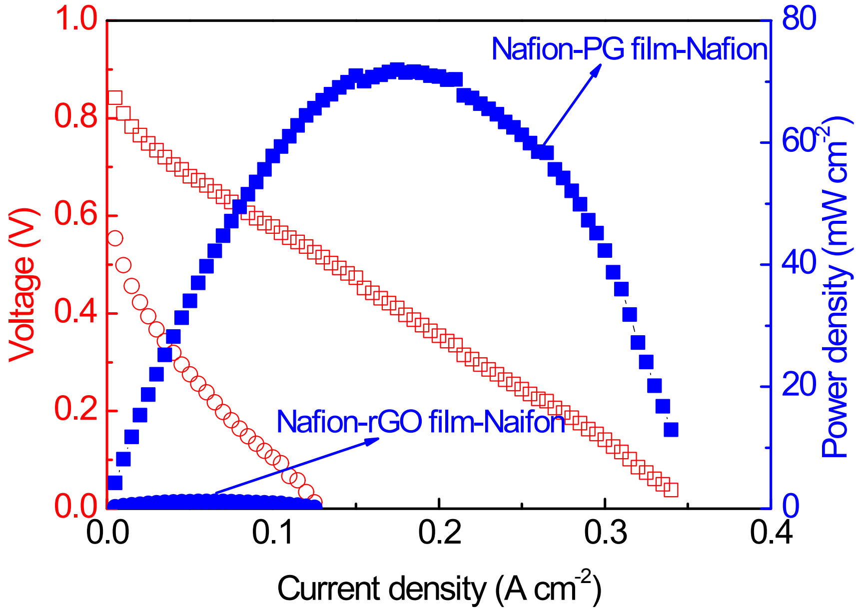

Fig. S8. Single cell performance of the Nafion-PG film-Nafion and Nafion-rGO film-Nafion composite membrane.

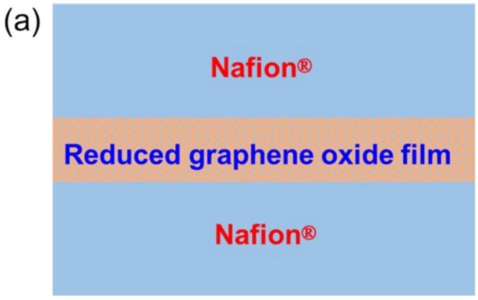

Fig. S9. Schematic illustration of sandwiched membrane using rGO films.

In addition, the conduction behavior of PGM and rGO was investigated by two probe electrochemical impedance spectroscopy (EIS) using an impedance/gain-phase analyzer (PARSTAT4000) in the frequency range from 1 MHz to 0.1 Hz with a voltage amplitude of 10 mV. Two platinum sheets are attached on the both sides of the sample by conductive silver ink and the samples were set in a thermostatic and humidistatic chamber (90%RH and 35°C). The Nyquist plot and bode plot of PGM are shown in **Fig. S10a, b**, which confirms that PGM is a mixed electron/proton conductive material.[8, 9] The equivalent circuit of this mixed conductor can be simplified as a parallel combination of electronic resistance (Re), and protonic resistance (Rp), which is in serial with a capacitor (C). In this case, the intersection of high frequency line with the real axis corresponds to the parallel of electronic and protonic resistance (RpRe/(Rp+Re)), and the intersection of low frequency is the electronic resistance (Re). **Fig. S10c, d** exhibits the typical electrochemical impedance spectra of rGO in the form of Nyquist plot and bode plot, respectively. The Nyquist plot of rGO gives an inductive line indicating that rGO is almost an electronic conductor with a little proton conduction.[6-8]

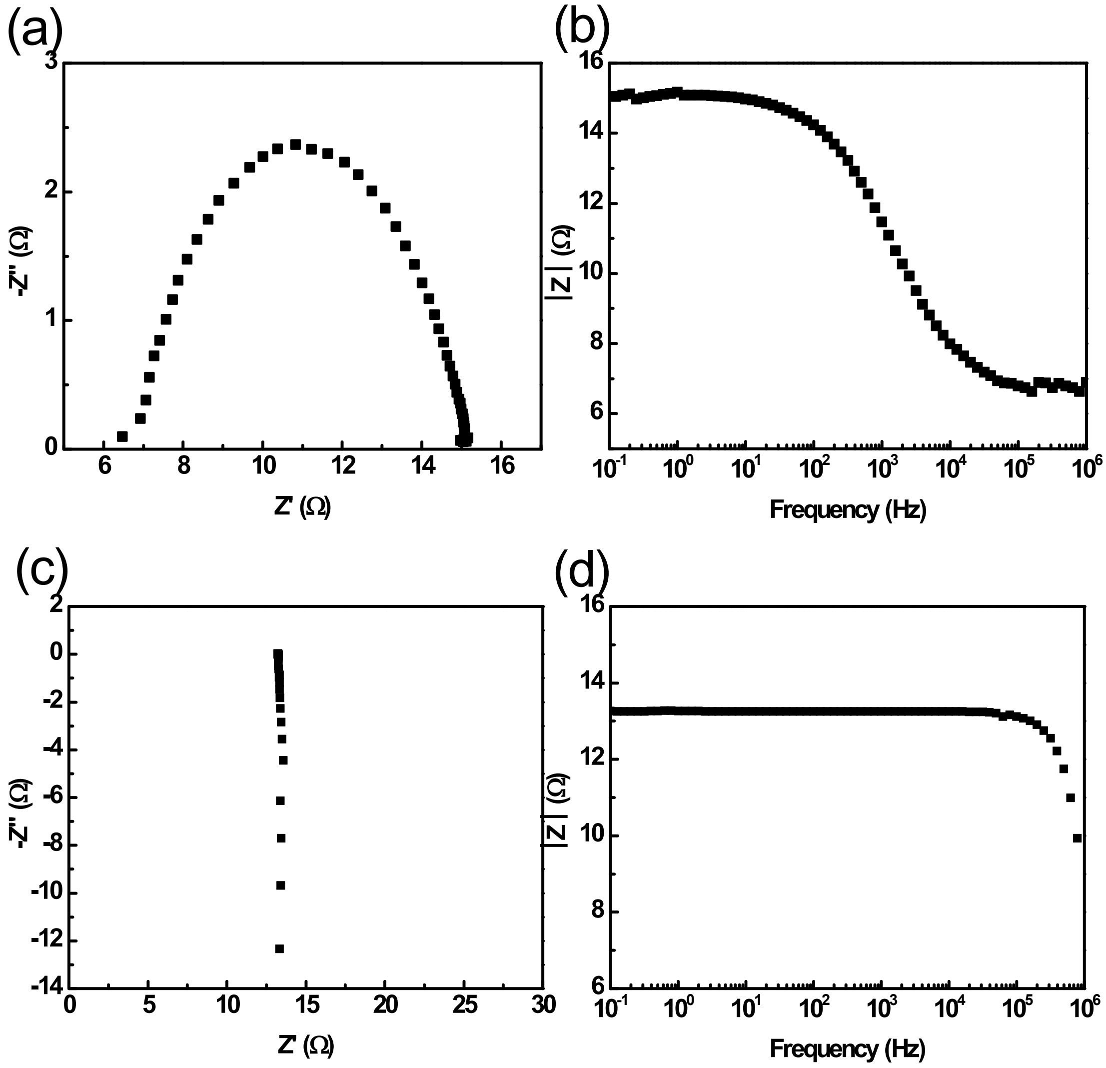

Fig. S10. Nyquist plot (a) and bode plot (b) of PGM; Nyquist plot (c) and bode plot (d) of rGO.

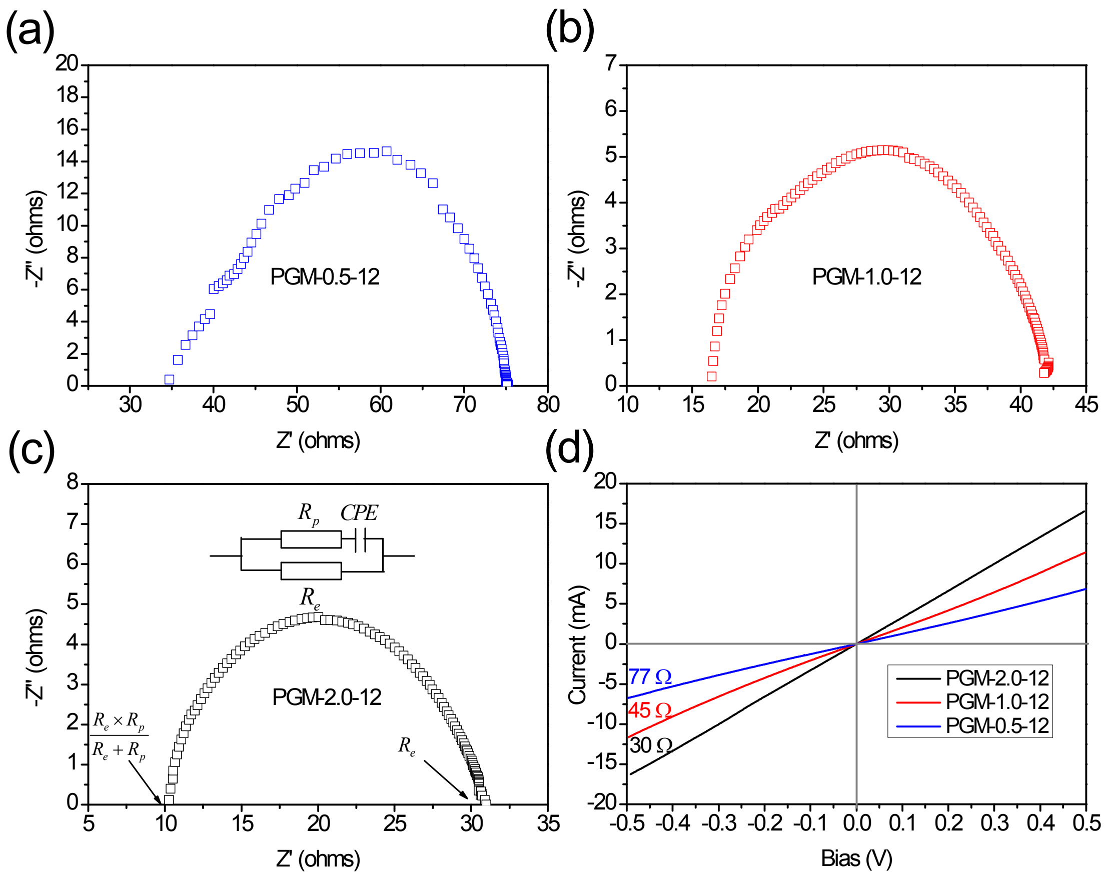

Fig. S11. Nyquist plots (by AC measurement techniques) of PGM with different experimental parameters: a) PGM-0.5-12; b) PGM-1.0-12; c) PGM-2.0-12; and d) the corresponding I-V curves by two-probe DC method at 90% RH and 35 °C. According to the equivalent circuit, the intersection of the high frequency line with the real axis was the resistance of the proton resistance and electron resistance in parallel ($\frac{R_e \times R_p}{R_e + R_p}$), and the intersection of the low-frequency line with the real axis was the electron resistance (R_e). The electron resistances of PGM obtained by I–V curves and Nyquist plots are quite close.

Table S1 P and O contents of PGM-1-y with different reaction time (results from XPS)

Reaction time (h)	0	8	12	16	24	30
P (wt%)	0	6.6	9.3	9.8	10.1	10.1
O (wt%)	-	27.5	42.1	42.2	40.1	40.1

the ATMP plays two roles in the reaction: 1) introducing phosphate groups into the materials, which can offer the material with proton-conducting feature; 2) at the same time, reducing graphene oxide. The graphene oxide can be reduced by the tertiary amino groups in ATMP during the hydrothermal reaction, resulting in an enhanced electron conductivity.[10-12] As shown in **Fig. S12**, the GO solution is gradually reduced into rGO under 90°C, showing an increasing electron conductivity with reaction time (from 4 to 24h, **Fig. S13**). In addition, the triethylamine (the chemical structure of triethylamine is very similar to ATMP) is used to investigate the reduction process of GO (**Fig. S14**). The electron conductivity of Tri-rGO films increases with the reaction time, and the value can reach 0.32 S cm^{-1} after 24h, as shown in **Fig. S15**. These two experiments suggests that the GO solution can be highly reduced by ATMP in the system, which indicates that the reaction with ATMP can introduce electronic conduction.

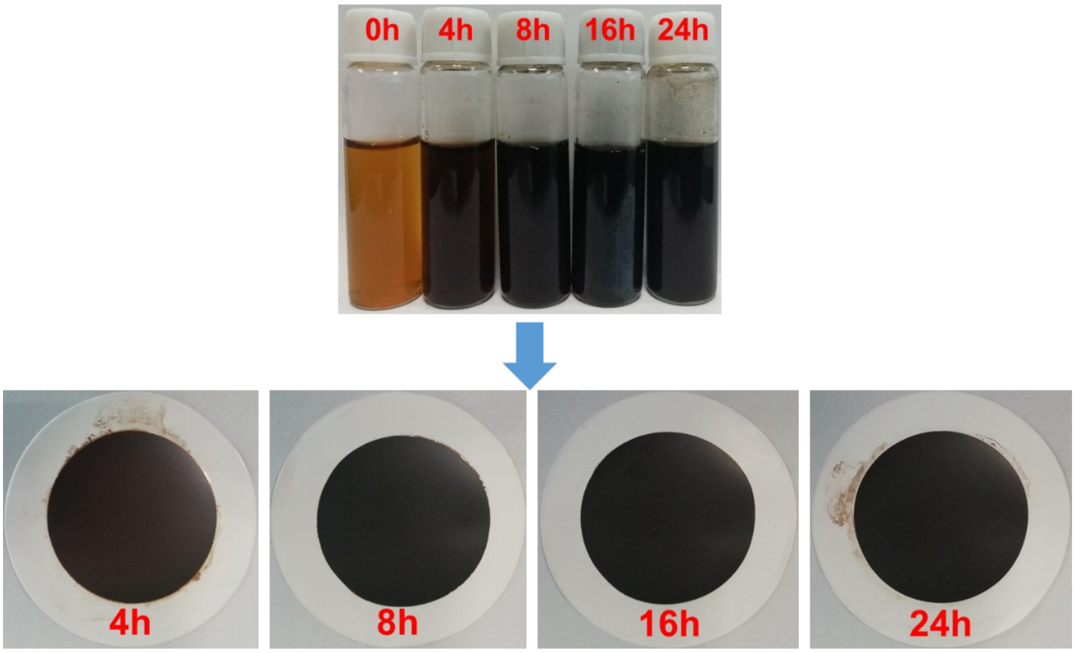

Fig. S12. The optical photograph of thermally reduced graphene oxide (Thermal-rGO) aqueous solution at various reaction times and the corresponding Thermal-rGO films.

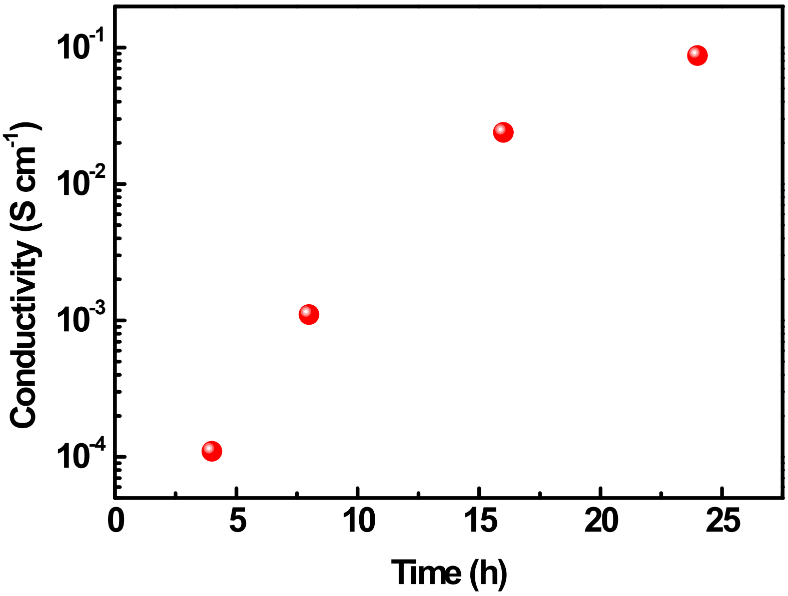

Fig. S13.The electron conductivity of Thermal-rGO films at various times.

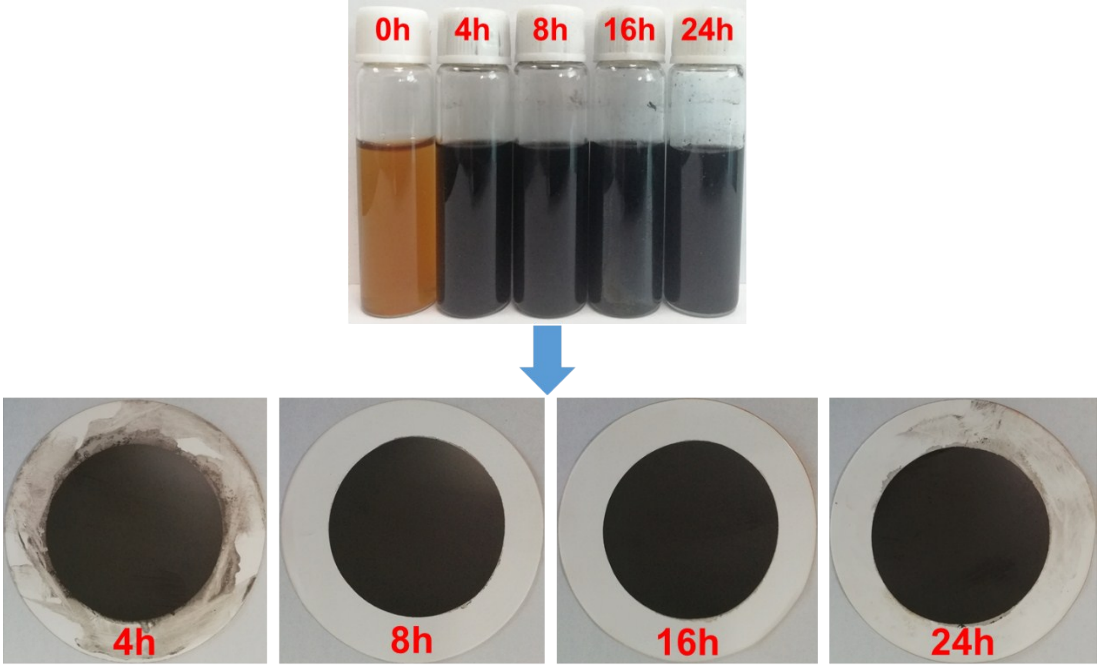

Fig. S14. The optical photograph of reduced graphene oxide aqueous solution by triethylamine (Tri-rGO) at various reaction times and the corresponding Tri-rGO films.

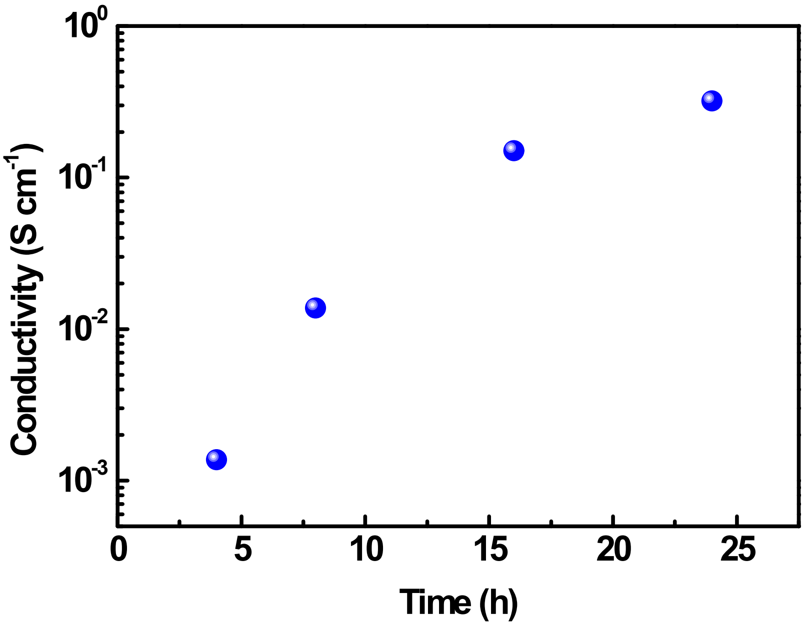

Fig. S15.The electron conductivity of Tri-rGO films at various times.

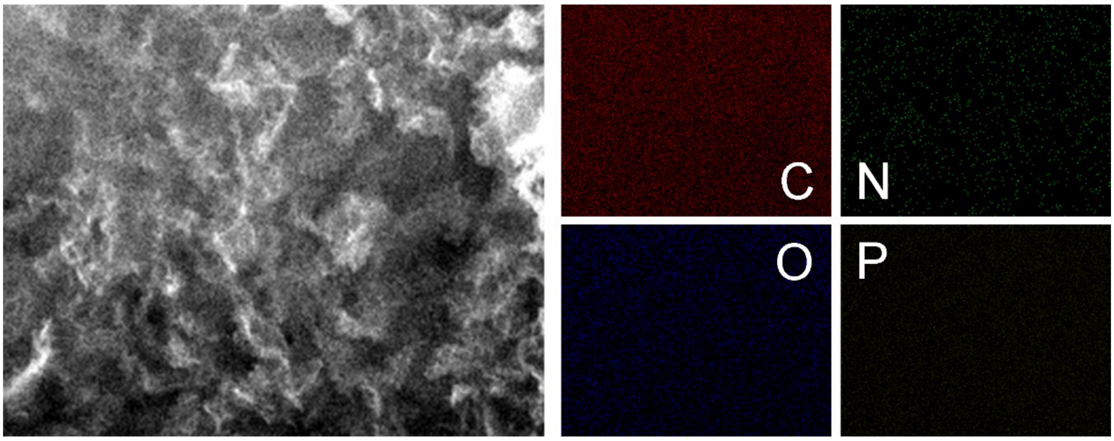

Fig. S16. The EDX mapping of C, N, O and P elements in the PGM.

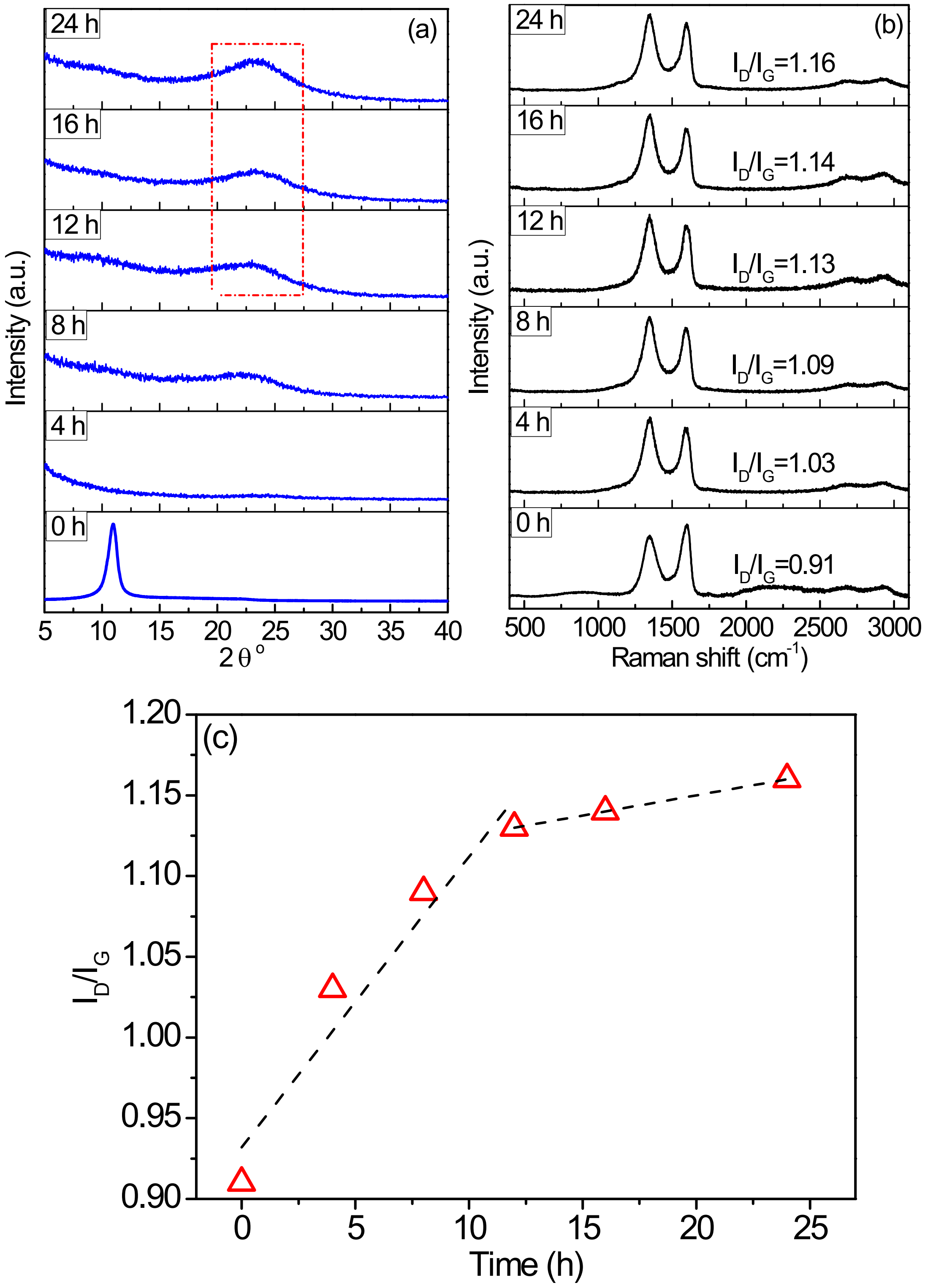

Fig. S17. a) XRD patterns; b) Raman spectra and c) I_D/I_G values of PGM at different reaction time.

The typical diffraction peak of GO appeared at around 11°, corresponding to a d_{001} spacing of 0.80 nm. At early stage (reaction time < 12h), no diffraction peaks of PGM were detected, suggesting that PG nanosheets were microscopically corrugated in the cell walls. Upon extending the reaction time (reaction time > 12h), a broad peak at around 23° ($d_{(002)}$=0.39 nm) was observed. This result appeared to suggest that graphite-like structure in each cell wall was formed only at the contacting points of corrugated rGO nanosheets via π-π stacking. The contacting points increased with the reaction time, presenting a slightly pronounced XRD peak at around 23°. These contacting points were in favor of the electron transport between the adjacent PG layers, which supported the enhancement of electron conductivity of PGM.

Figure S8b presented the Raman spectra of PGM at different reaction times. During the reduction process, ATMP was bonded onto rGO nanosheets and the structural defect led to an increased I_D/I_G ratio. Interestingly, the I_D/I_G value remarkably increased from 0.91 to 1.13 at first 12h, and then showed a little increase in I_D/I_G value from 1.13 to 1.16 for the next 12h. It indicated that the reaction between ATMP and GO seems to be completed in 12h. This result was in accord with the XPS data with a little change in P contents of PGM after 12h (Table S1). XPS, XRD and Raman results suggested that at early reduction stage, phosphate groups were gradually introduced in PGM until the reaction between ATMP and GO was accomplished. The phosphate groups in PGM provide more proton transport sites. Consequently, the PGM presented a higher proton conductivity than electron conductivity. Extending reaction time only led to the further reduction of GO, which significantly enhanced the electron conductivity of PGM.

Table S2 Comparison of the mixed conductivity of the present PGM and other graphene-based MIEC.

Materials	Proton conductivity ($S\ cm^{-1}$)	Electron conductivity ($S\ cm^{-1}$)	Ref.
Chemical reduced GO	—	10^{-1}–10^{2}	[13]
Ozonated GO film	3×10^{-4} (25 °C, 30%RH)	—	[14]
	2.5×10^{-2} (25 °C, 95%RH)	—	
Sulfonated GO film	2.0×10^{-2} (22 °C, 100%RH)	—	[15]
	5.8×10^{-2} (55 °C, 100%RH)	—	
Single-layer GO	~10^{-6} (25 °C, 60%RH)	—	[16]
Multilayer GO	~10^{-4} (25 °C, 60%RH)	—	
Polyoxometalate-Modified	2.4×10^{-2} (25 °C, 60%RH)	—	[17]
GO monolith	1.0×10^{-2} (80 °C, 60%RH)	—	
GO film	2.8×10^{-2} (25 °C, 88%RH)	—	[18]
GO bulk sample	~10^{-7} (27°C, 98%RH)	—	[19]
Reduced GO film	3.0×10^{-2} (25 °C, 90%RH)	1.0×10^{-3} (25 °C, 90%RH)	[20]
intercalated SO_4^{-2}	2.0×10^{-2} (25 °C, 90%RH)	2.0×10^{-2} (25 °C, 90%RH)	
Photo-reduced GO film	6.0×10^{-4} (25 °C, 90%RH)	6.0×10^{-4} (25 °C, 90%RH)	[21]
	~10^{-6} (25 °C, 40%RH)	~10^{-6} (25 °C, 40%RH)	
Thermal reduced GO film	5.0×10^{-5} (25 °C, 90%RH)	5.0×10^{-5} (25 °C, 90%RH)	
	~10^{-8} (25 °C, 40%RH)	~10^{-8} (25 °C, 40%RH)	
GO film	5.0×10^{-3} (90 °C, 100%RH)	7.4×10^{-3} (80 °C, 0%RH)	[22]
Nafion/CNT membranes	1.0×10^{-3} (25 °C, 100%RH)	10^{-7}–10^{-4} (25 °C, 100%RH)	[23]
Perovskite-type oxides	10^{-6}–10^{-3} (650 °C)	10^{-6}–10^{-3} (650 °C)	[24]
Oxygen functionalized few-layer graphene	8.7×10^{-3} (80 °C, 95%RH)	1.0×10^{-1} (80 °C, 95%RH)	[25]
PGM-1-12	**3.6×10^{-2}** (80 °C, 60%RH)	**1.2×10^{-1}** (80 °C, 60%RH)	**This work**
PGM-1-24	**1.3×10^{-1}** (35 °C, 98%RH)	**2.56×10^{-1}** (35 °C, 98%RH)	
PGM-2-16	**8.5×10^{-2}** (35 °C, 90%RH)	**2.74×10^{-1}** (35 °C, 90%RH)	
PGM-2-16	**5.5×10^{-3}** (35 °C, 40%RH)	**2.74×10^{-1}** (35 °C, 40%RH)	

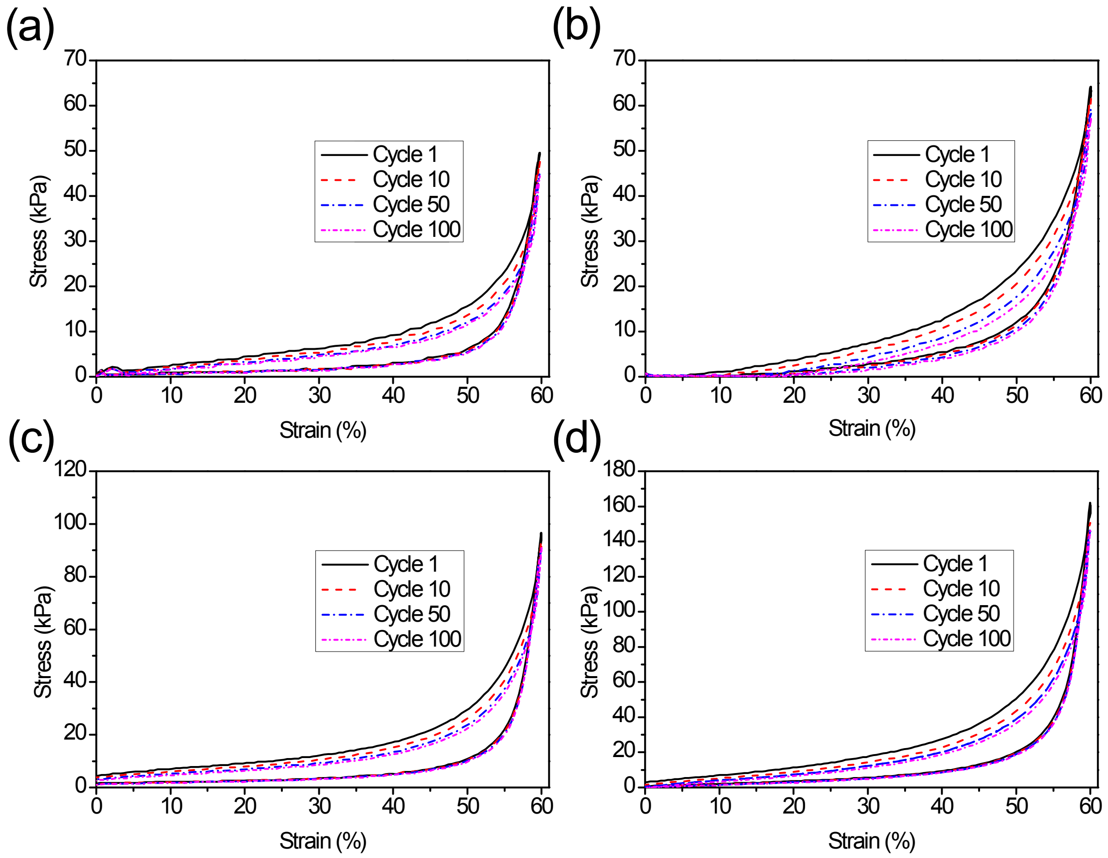

Fig. S18. The stress–strain curves of PGM prepared via different initial GO solutions: (a) 2 mg mL^{-1}, (b) 4 mg mL^{-1}, (c) 6 mg mL^{-1}, (d) 8 mg mL^{-1}.

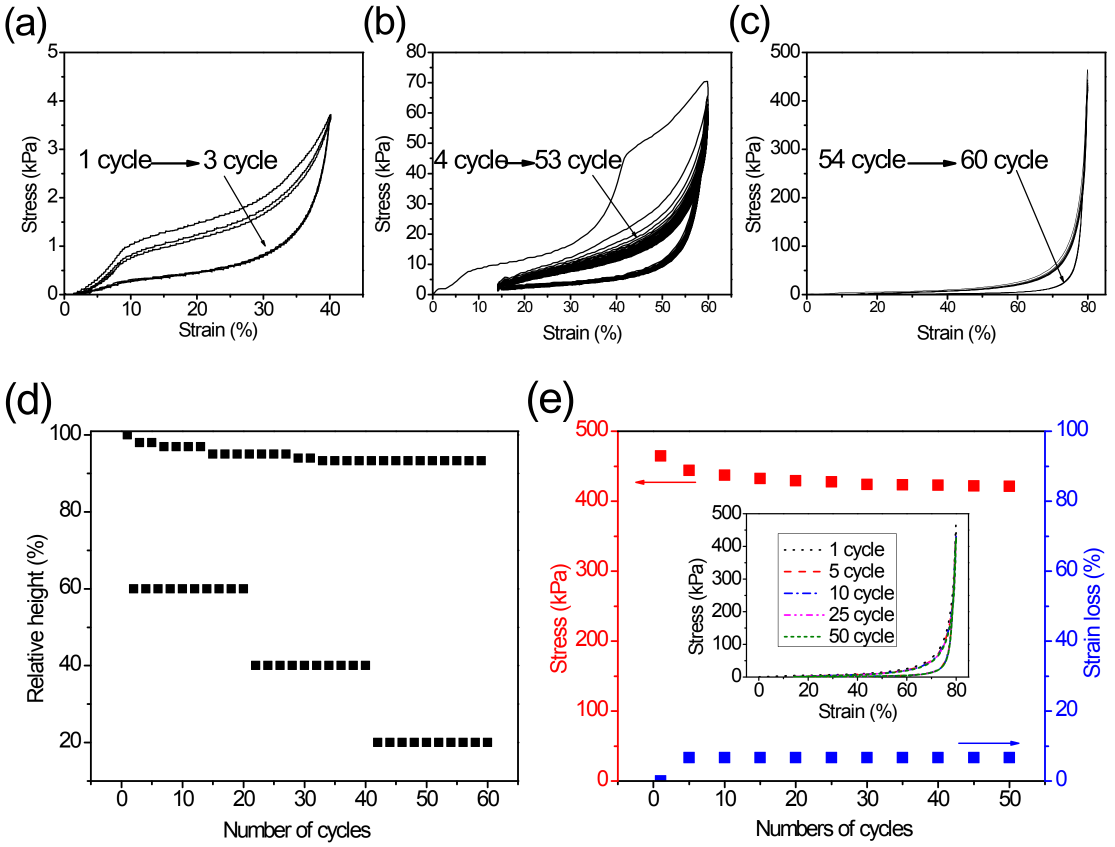

Fig. S19. The stress–strain curves of PGM-1-12 during continuous cycling tests at various strains: (a) 40% of strain; (b) 60% of strain; (c) 80% of strain; (d) Changes in relative height of the PGM when repeatedly compressed to 40%, 60% and 80% of strain for 60 cycles; (e) The ultimate stress and strain loss coefficient for 50 cycles. Inset: the stress-strain curves of PGM-1-12 at a strain of 80% for 50 cycles.

Reference:

1. G. A. Pilgrim, J. W. Leadbetter, F. Qiu, A. J. Siitonen, S. M. Pilgrim and T. D. Krauss, *Nano Lett.* , 2014, **14**, 1728-1733.
2. M. R. Karim, K. Hatakeyama, M. Koinuma and S. Hayami, *J. Mater. Chem. A*, 2017, **5**, 7243-7256.

3. K. Hatakeyama, M. S. Islam, K. Michio, C. Ogata, T. Taniguchi, A. Funatsu, T. Kida, S. Hayami and Y. Matsumoto, *J. Mater. Chem. A*, 2015, **3**, 20892-20895.

4. K. Hatakeyama, C. Ogata, M. Koinuma, T. Taniguchi, S. Hayami, K. Kuroiwa and Y. Matsumoto, *ACS Appl. Mat. Interfaces* 2015, **7**, 23041-23046.

5. M. S. Islam, M. R. Karim, K. Hatakeyama, H. Takehira, R. Ohtani, M. Nakamura, M. Koinuma and S. Hayami, *Chemistry – An Asian Journal*, 2016, **11**, 2322-2327.

6. K. Hatakeyama, H. Tateishi, T. Taniguchi, M. Koinuma, T. Kida, S. Hayami, H. Yokoi and Y. Matsumoto, Chem. Mater. , 2014, **26**, 5598-5604.

7. M. R. Karim, K. Hatakeyama, M. Koinuma and S. Hayami, J. Mater. Chem. A, 2017, **5**, 7243-7256.

8. Y. Wang, C. Zhu, R. Pfattner, H. Yan, L. Jin, S. Chen, F. Molina-Lopez, F. Lissel, J. Liu, N. I. Rabiah, Z. Chen, J. W. Chung, C. Linder, M. F. Toney, B. Murmann and Z. Bao, *Science Advances*, 2017, **3**.

9. T. Bayer, S. R. Bishop, N. H. Perry, K. Sasaki and S. M. Lyth, *ACS Appl. Mat. Interfaces* 2016, **8**, 11466-11475.

10. C. K. Chua and M. Pumera, *Chem. Soc. Rev.* , 2014, **43**, 291-312.

11. S. Zhang, Y. Shao, H. Liao, M. H. Engelhard, G. Yin and Y. Lin, *ACS Nano*, 2011, **5**, 1785-1791.

12. M. Mrlík, M. Ilčíková, T. Plachý, V. Pavlínek, Z. Špitalský and J. Mosnáček, *Chem. Eng. J.* , 2016, **283**, 717-720.

13. C. K. Chua and M. Pumera, *Chem. Soc. Rev.* , 2014, **43**, 291-312.

14. W. Gao, G. Wu, M. T. Janicke, D. A. Cullen, R. Mukundan, J. K. Baldwin, E. L. Brosha, C. Galande, P. M. Ajayan, K. L. More, A. M. Dattelbaum and P. Zelenay, *Angew. Chem. Int. Ed.* , 2014, **53**, 3588-3593.

15. G. Jiang, M. Goledzinowski, F. J. E. Comeau, H. Zarrin, G. Lui, J. Lenos, A. Veileux, G. Liu, J. Zhang, S. Hemmati, J. Qiao and Z. Chen, *Adv. Funct. Mater.* , 2016, **26**, 1729-1736.

16. K. Hatakeyama, M. R. Karim, C. Ogata, H. Tateishi, A. Funatsu, T. Taniguchi, M. Koinuma, S. Hayami and Y. Matsumoto, *Angew. Chem. Int. Ed.* , 2014, **53**, 6997-7000.
17. Y. Liu, S. Liu, X. Lai, J. Miao, D. He, N. Li, F. Luo, Z. Shi and S. Liu, *Adv. Funct. Mater.* , 2015, **25**, 4480-4485.
18. W. Gao, N. Singh, L. Song, Z. Liu, A. L. M. Reddy, L. Ci, R. Vajtai, Q. Zhang, B. Wei and P. M. Ajayan, *Nat. Nanotechnol.* , 2011, **6**, 496-500.
19. M. R. Karim, K. Hatakeyama, T. Matsui, H. Takehira, T. Taniguchi, M. Koinuma, Y. Matsumoto, T. Akutagawa, T. Nakamura, S.-i. Noro, T. Yamada, H. Kitagawa and S. Hayami, *J. Am. Chem. Soc.* , 2013, **135**, 8097-8100.
20. K. Hatakeyama, M. S. Islam, K. Michio, C. Ogata, T. Taniguchi, A. Funatsu, T. Kida, S. Hayami and Y. Matsumoto, *J. Mater. Chem. A*, 2015, **3**, 20892-20895.
21. K. Hatakeyama, H. Tateishi, T. Taniguchi, M. Koinuma, T. Kida, S. Hayami, H. Yokoi and Y. Matsumoto, *Chem. Mater.* , 2014, **26**, 5598-5604.
22. T. Bayer, S. R. Bishop, N. H. Perry, K. Sasaki and S. M. Lyth, *ACS Appl. Mat. Interfaces* 2016, **8**, 11466-11475.
23. V. Ijeri, L. Cappelletto, S. Bianco, M. Tortello, P. Spinelli and E. Tresso, *J. Membr. Sci.* , 2010, **363**, 265-270.
24. S. Escolástico, S. Somacescu and J. M. Serra, *Chem. Mater.* , 2014, **26**, 982-992.
25. C. Singh, N. S, A. Jana, A. K. Mishra and A. Paul, *Chem. Commun.* , 2016, **52**, 12661-12664.